This article has been accepted for publication in a future issue of this journal, but has not been fully edited. Content may change prior to final publication. Citation information: DOI 10.1109/TAP.2020.3027042, IEEE Transactions on Antennas and Propagation

A Single-Layer Low-Profile Broadband Metasurface Antenna Array for Sub-6 GHz 5G Communication Systems

J.D Ntawangaheza, *Liguo Sun, Zipeng Xie*, Yingyang Pang, Zhuo Zheng, and Gerard Rushingabigwi

***Abstract*—This paper presents a planar, low-profile, and single-layer metasurface-based wideband 4×4 array antenna operating in the 5G sub 6 GHz. The proposed antenna consists of a 4×4 unequal size metasurface unit cells fed by a simple parallel microstrip feed network in the form of a thin strip cross dipole. The wide impedance bandwidth (IBW) and improved boresight gain characteristics are realized due respectively to the excitation of multiple TM resonance modes that are closely spaced and the relatively large lateral size that supports in-phase currents. With an overall size of $1.40\lambda_0 \times 1.22\lambda_0 \times 0.054\lambda_0$ (where λ_0 is the free-space wavelength at the center frequency of 5.64 GHz), the proposed antenna realizes an IBW of 41.13% (4.48-6.80 GHz), a peak boresight gain of 10.14 dBi, low cross-polarization in the E- and H-planes and higher front-to-back ratio. Because of the advantages of low profile, planar and single-layer structure, as well as equal E- and H-planes 3-dB beamwidth, the proposed antenna is a competitive candidate for several modern wireless communications systems, including 5G in the sub 6 GHz.**

***Index Terms*—Artificial magnetic conductor, broadband, cross-polarization, front-to-back ratio, high gain, metasurface, a microstrip patch antenna, magneto-electric dipole, wideband antenna.**

I. Introduction

Like its predecessors, 5G wireless communication systems require antennas with attractive features, such as low-profile, compact size, high gain, low cost, easy integration, and wide operating frequency bandwidth (BW) to increase data transmission rate and communication distance while reducing considerably the size and volume of the systems.

Although the low-profile, easy integration and miniaturized-size requirements can be easily realized using an ordinary microstrip patch antenna (MPA) excited at the fundamental mode, it suffers from the inherent problem of narrow BW (<5%) and low gain ($\sim$6 dBi) [1]. Over the past several decades, several techniques have been proposed to circumvent the narrow impedance (I) BW drawback of the patch antenna, including the use of multiple resonators in stacked [2] or coplanar configurations [3], use of thick, low relative permittivity (ε_r) substrate and cutting slots or slits on the surface of the patch [4]. These IBW enhancement methods can achieve wider BWs and moderate gains, but at the cost of increased antenna lateral size, volume, and fabrication cost. Besides, coplanar multi-resonator [3] and thick substrates [4] methods yield pattern squint over the IBW [3] and high cross-polarization (X-pol) level in the H-plane at the upper-frequency band, respectively.

Wider IBWs and improved gain characteristics can be obtained by placing a patch antenna [5]-[10] or dipole antenna [11]-[16] above or under an artificial magnetic conductor ground plane (AMC-GND). The enlarged IBW and high gain characteristics of these antennas are due to the excitation of multiple TM surface waves (SWs) that are closely spaced and increased antenna radiating aperture, respectively. However, not only dipole antennas require differential feeds and high substrate heights ($> 0.1\lambda_0$), but also the IBWs of [12], [14]-[16] are less than 30%. In general, recently published linearly polarized microstrip patch antennas (LPMPAs) over the AMC-GND have narrower IBWS (<30%) [4] and [6]-[10].

Metasurface (MTS) structures have also been integrated with slot antennas [17]-[25] to improve their BWs and gains. However, the IBWs of the MTS-based slot antennas in [17]-[20], [23], and [25] are relatively narrow (<30%). What is more, slot antennas generally exhibit low front-to-back ratios (FBR) [17]. The latter can be enhanced using a perfect electric conductor (PEC) cavity, an AMC reflector [19], or using an L-shaped probe feeding approach [21], but at the expense of increased design complexity, volume, cost, and high X-pol.

In all of the above references, multilayer configurations have been employed to achieve wider IBWs and higher gains characteristics with the disadvantages of the increased antenna size and volume, design complexity, and cost. There are a few single-layer metasurfaces or AMC-based antennas available in the open literature [26]-[30]. While antennas in [27], [30] are single-layer, simple to model and fabricate, their IBWs and profiles are, respectively, 13% and 27%, and $0.05\lambda_0$ and

Manuscript received xx yy, 2020; revised xx yy, 2020; accepted xx yy, 2020. Date of publication xx yy, 2020; date of current version xx yy, 2020. This work was supported by the Chinese Scholarship Council (corresponding author: Liguo Sun.)

The authors are with the department of Electronic Engineering and Information Science, University of Science and Technology of China (USTC), Hefei 23006, China (e-mail: ntajado@mail.ustc.edu.cn; liguos@ustc.edu.cn, xzp1993@mail.ustc.edu.cn;yingyp@mail.ustc.edu.cn;zhuozhen@mail.ustc.edu.cn; gerardrushingabigwi@yahoo.com)

This article has been accepted for publication in a future issue of this journal, but has not been fully edited. Content may change prior to final publication. Citation information: DOI 10.1109/TAP.2020.3027042, IEEE Transactions on Antennas and Propagation

$0.74\lambda_0$. The antenna proposed in [29] to overcome the low FBR of metasurface-based slot antennas has a complex configuration and an IBW of only 26%, while its profile is $0.07\lambda_0$.

In this paper, a planar, single-layer, low-profile, and wide IBW 4×4 metasurface-based antenna array is proposed to overcome the previously mentioned burdens of early works in terms of the profile, size, IBW, X-pol, FBR and the number of the substrates used in the design of AMC-based antennas. The newly designed antenna can also be used to mitigate the high profile ($0.25\lambda_0$, whereλ_0 is the free-space wavelength at the center of the operating frequency band) of conventional magneto-electric dipole antennas [31]. The proposed antenna comprises a 4×4 unequal size metasurface unit cells fed by a corporate microstrip line feed network in the form of a thin strip cross dipole. The presented antenna has several salient features, including a wide IBW of 41.13% (4.48-6.80 GHz), wider 3-dB gain BW with a peak gain of 10.14 dBi at 6.3 GHz, low X-pol and high FPR in the E- and H-planes, stable broadside patterns with identical 3-dB beamwidths in the two principal planes, planar and simple structure.

II. Antenna Structure, Design Theory, Procedure And Comparison, And Performance analysis

A. Antenna Structure

Fig. 1(a)-(b) illustrates the top and side view of the proposed single-layer, low-profile, and wideband MTS-based 4×4 antenna array. The proposed antenna consists of 16 unequal size unit cells arranged in a 4×4 antenna array configuration. A single-layer dielectric substrate with a thickness of $H = 3$ mm and a relative dielectric constant of ($\varepsilon_r = 2.65$) is used to print both the MTS unit cells and the microstrip line feed network on the same top face.

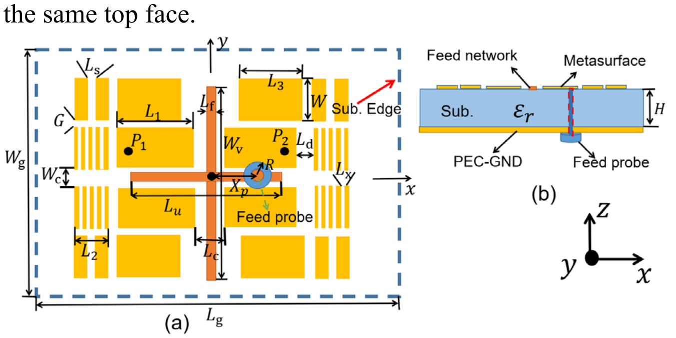

Fig. 1. The proposed antenna structure: (a) top view, (b) side view: $L_1 = 14.7$, $L_2 = 11$, $L_3 = 11.6$, $L_u = 13.9$, $L_d = 2$, $L_s = 0.2$, $L_x = 0.1$, $L_f = 1.1$, $L_c = 4.8$, $W = 11$, $W_c = 1.7$, $G = 1$, $W_v = 43.2$, $W_g = 68$, $L_g = 75$ and $R = 2.7$ (unit: mm)

The feed network, which has the same thickness as the 16 MTS unit cells (0.035 mm), is a simple corporate microstrip line feeding structure. The input signal from the feed coaxial probe is equally split into four outputs. Since there is no direct contact between the antenna and the feed lines, the proposed feeding scheme can be considered a hybrid of the microstrip line and proximity feeding techniques. It can be found in Fig. 1(a) that the feed network is asymmetric in the x direction ($X_p \neq 0$), meaning the elements located in the positive (+) and (−) negative x directions will experience different phase shifts, and this may lead to beam steering over the operating frequency band. To resolve this problem, the phase of the scattered fields from the elements located in the $+x$ direction, right near the feeding probe, are delayed using L_d parameter so that the phase difference ($\nabla\psi = 2\pi(P_1 - P_2)/\lambda_0$) of the AMC unit cells in the $+x$ and $-x$ directions is negligible. It should be noted that the two points denoted as P_1 and P_2 are used to explain the difference in the current path of the MTS unit cells located in the + and $-x$ directions.

It can also be seen in Fig. 1(a) that the peripheral MTS unit cells located along the x direction are sliced into smaller unit cells using L_s and L_x parameters to respectively improve the impedance matching and reduce the antenna size (in terms of λ_0) at the upper-frequency band edge. The inner two patches are cut into five small cells of nearly equal width. The reduction in the antenna size at higher frequencies results in reduced sidelobe levels (SSLs) in the E-plane. However, the use of large L_d, L_s and L_x leads to a poor impedance matching due to the reduced coupling among metasurface unit cells, and a circular stub (pad) with a radius (R) is utilized to control the impedance matching of the final design. The latter is shown in Fig. 1(a) using a blue circular ring. The pad also helps in welding the coaxial line to the microstrip feed line. The optimized antenna parameter dimensions are shown in the caption of Fig. 1.

B. Design Theory

The design philosophy of the presented metasurface-based 4×4 antenna array is relatively straightforward. It is well known that an MPA has a high resonance resistance at the edges, as shown in (1) [32] and Fig. 2(b). To obtain a good impedance matching, the proposed antenna utilizes a feed network with a high characteristic impedance, as shown in (2).

$$R_a = \frac{90 \cdot \varepsilon_r^2}{\varepsilon_r - 1}\left(\frac{L}{W}\right)^2 cos^2\left(\frac{\pi \cdot \Delta x}{L}\right) \quad (1)$$

In equation (1), ε_r, L, W, and Δx are, respectively, the relative permittivity of the supporting substrate, length and the width of the rectangular microstrip patch (RMPA), and the distance of the feed probe with respect to the patch width edge. As observed in equation (1), for a square-shaped patch excited at its edges, R_a is maximum and solely depends on ε_r.

$$Z_n = n \cdot Z_s \quad (2)$$

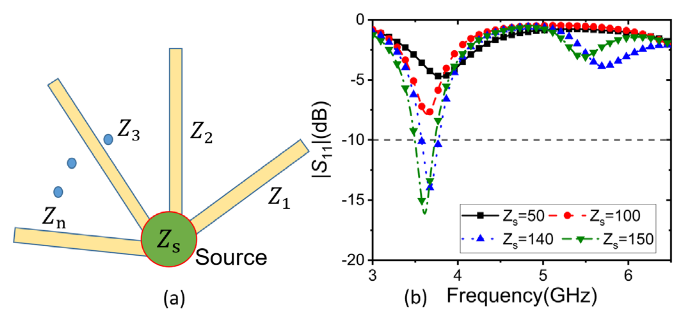

Fig. 2. (a) A schematic diagram showing a parallel feed network with n equal power divisions, (b) simulated $|S_{11}|$of an edge-fed square patch with feed lines of characteristic impedances (Z_s) shown in the legend. Unit is Ω.

On the other hand, the characteristic impedance of the feed lines

This article has been accepted for publication in a future issue of this journal, but has not been fully edited. Content may change prior to final publication. Citation information: DOI 10.1109/TAP.2020.3027042, IEEE Transactions on Antennas and Propagation

of an N-way parallel feed network with equal power division shown in Fig. 2(a) can be calculated using equation (2) [33]. As observed from equation (2), for a 4-way equal power split feed network, if the source has a characteristic impedance of 50 Ω, the output feed lines will have characteristic impedances of approximately 200 Ω, which reasonably match the high resonance resistance of the patch, as shown in Fig. 2(b).

C. Design Procedure and Performance Comparison

The proposed antenna can also be viewed as a grid-slotted patch [20], and therefore, to understand how it achieves good impedance and radiation characteristics, a performance comparison is made between five different antennas.

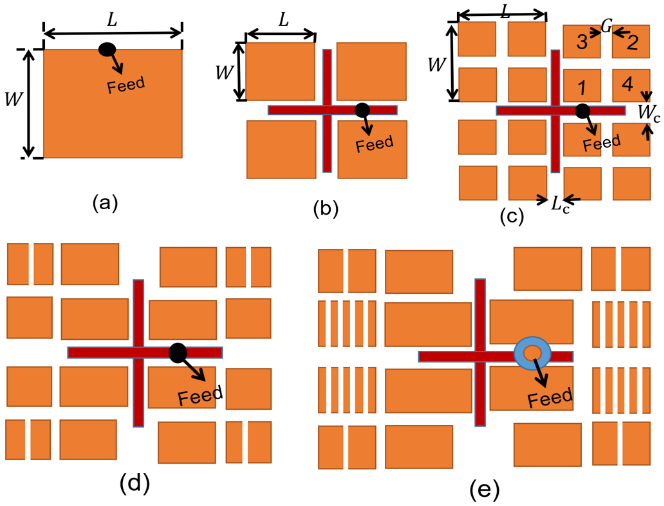

Fig. 3. The proposed antenna evolution process: (a) ant1, (b) ant2, (c) ant3, (d) ant4 and (e) ant5 (proposed), respectively. The values of G, W, and L are 0.5,23 and 23 mm, respectively, while those of W_c and L_c vary with the width of the feed cross dipole.

These 5 antennas are: 1) a square patch with a length of $L = W = 23$ mm fed at its edge with feed lines of different characteristic impedances; 2) a 2×2 antenna array consisting of four patches with dimensions of $L = W = 23$ mm fed by two orthogonal thin microstrip lines network; 3) a 4×4 MTS-based antenna array with small equal square patches obtained by equally slicing the above square patch into four unit cells and also fed by the two orthogonal thin microstrip line network; 4) a 4×4 MTS-based antenna array with unequal size unit cells fed by the same aforementioned microstrip line feed structure and with only L_s parameter; 5) a 4×4 MTS-based antenna array with unequal size patches fed by the two orthogonal microstrip line feed structure and with parameters L_d, L_s and L_x. These five antennas are schematically shown in Fig. 3(a)-(e), and are, respectively, hereafter named ant1, ant2, ant3, ant4, and ant5 (proposed). It should be noted that a circular stub of radius (R) is used to tune the proposed antenna impedance matching. It is important to mention that ant1 is designed to resonate at around 3.5 GHz, which lies in the lower band of the 5G in the sub-6GHz band.

The simulated $|S_{11}|$ and 3D radiation pattern of ant1 at 3.7 GHz are shown in Figs. 2(b) and 4(c), respectively, while those of ant2 are illustrated in Fig. 4(a)-(b), (d)-(e), respectively. As seen in Fig. 2(b), the 50 Ω edge-fed square patch has a poor impedance matching at 3.81 GHz due to the high resonance resistance at the edge, as shown in (1). However, when Z_s is varied to 100 Ω, 140 Ω and 150 Ω, the antenna impedance matching gets progressively better and realizes a $|S_{11}| < -10$ dB IBW of 5.86% for 150 Ω. As a result, the initial microstrip feed line width (L_f) was chosen to be between 0.8 mm and 0.9 mm. This corresponds to the characteristic impedances of $140 - 135$ Ω using the substrate with the properties mentioned previously. Ant1 achieved a maximum gain of 7.61 dBi at 3.7 GHz, as shown in Fig. 4(c).

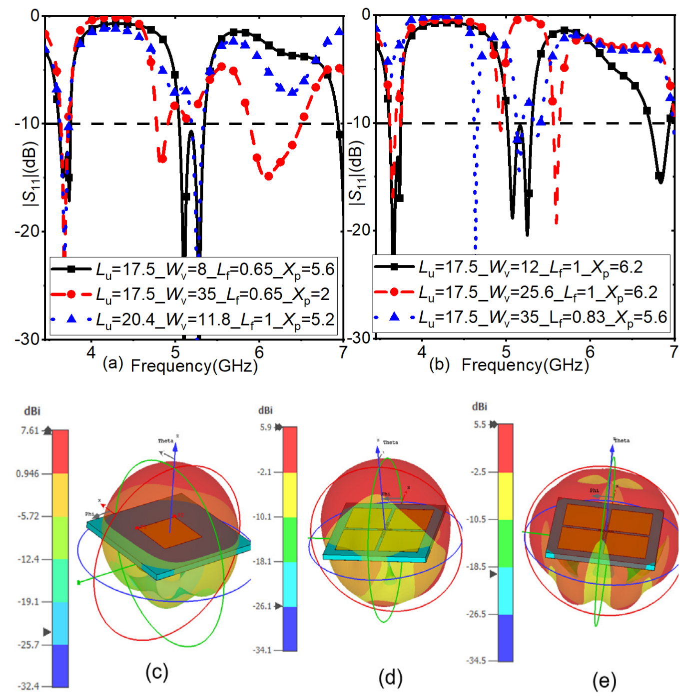

Fig. 4. (a)-(b) simulated $|S_{11}|$of ant2; (c) simulated 3D pattern of ant1 at 3.7GHz; and (e) and (e) simulated 3D patterns for ant2 at 3.7 GHz and 5.1 GHz, respectively. Unit is mm.

On the other hand, as illustrated in Fig. 4(a)-(b), depending on the dimensions of the feeding microstrip line and the position of the coaxial probe (X_p), ant2 can realize a dual-band behavior in the frequency ranges of 3.88% (3.61-3.75 GHz) and 5.78% (5.04-5.34 GHz). However, only the lower frequency band has an undistorted broadside pattern, whereas the upper-frequency band has a deteriorated radiation pattern with a null in the boresight, as can be found in Fig. 4(e). At 3.7 and 5.1 GHz, ant2 realized gains of 5.9 and 5.5 dBi, respectively, as illustrated in Fig. 4(d)-(e). The deterioration of the radiation pattern for ant2 at 5.1 GHz is due to its relatively large electrical size ($S > \lambda_0$) at the higher frequency, as can be seen in (3) [34] and (4) [35].

The equation (3) shows that the value of the resonance frequency for different TM SW modes depends on the size of the AMC surface ($P_{(x,y)}N_{(x,y)}$), while (4) indicates that the overall radiation pattern of the antenna is determined by the interaction of the in-phase and out-of-phase surface current portions on the antenna surface. The large size ($S > \lambda_0$) of the antenna will cause the currents on different parts of the antenna surface to undergo constructive and destructive interferences, leading to the radiation patterns with grating lobes (SSLs) and null in the broadside [35]-[36]. It is worth noting that the surface

This article has been accepted for publication in a future issue of this journal, but has not been fully edited. Content may change prior to final publication. Citation information: DOI 10.1109/TAP.2020.3027042, IEEE Transactions on Antennas and Propagation

current distribution on the surface of ant1 and ant2 is not shown for brevity.

$$\beta_{\mathrm{sw}(x,y)} P_{(x,y)} N_{(\mathrm{x,y})} = m\pi \,, m = 1,2,3, \ldots \tag{3}$$

$$\vec{E}=\vec{E}_0(a_0+a_1 e^{idk_x}+a_2\ e^{i2dk_x}+\ldots+a_n e^{indk_x} \tag{4}$$

Where in equation (3) $\beta_{\mathrm{sw}(x,y)}$, $P_{(x,y)}$, and $N_{(\mathrm{x,y})}$ represents, respectively, the propagation constant of the SW at resonance in the x or y direction, the metasurface unit cells periodicity, and the number of the MTS unit cells. In equation (4), a_{n}, d, and k_{x} denotes the magnitude of the current portions on the surface of the antenna, which can be in-phase or out-of-phase, the separation distance between current portions, and the wave number in the direction of the array axis (x in this study).

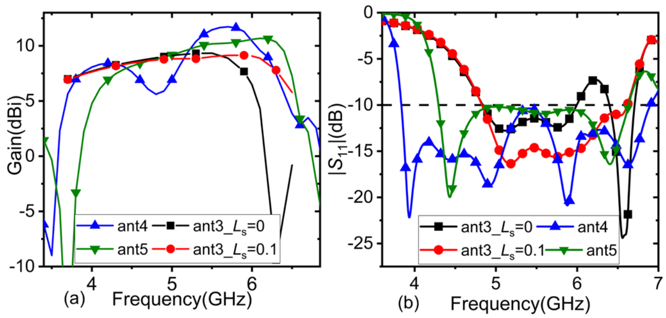

Fig. 5. (a) and (b) simulated boresight gain and $|S_{11}|$ of ant3, ant4 and ant5 (proposed), respectively. Note that the impact of L_{s} on the impedance matching at higher frequency band is also indicated. Unit is mm.

Fig. 5(b) shows that ant3 and ant4 achieved fractional IBWs of 31.46% (4.82-6.62 GHz) and 57.22% (3.83-6.90 GHz), whereas ant5 exhibited an IBW of 42.85% (4.29-6.63 GHz). The IBWs of ant3, ant4, and ant5 is more than five times, over nine times and higher than 7 times that of ant1, respectively. Moreover, ant3, ant4, and ant5 obtained boresight peak gains of 9.13 dBi at 5.5 GHz, 11.72 dBi at 5.7 GHz, and 10.67 dBi at 6.1 GHz. However, as observed in Fig. 5(a), ant4 has a dip valley in the boresight gain curve in the frequency range of 4-5 GHz as compared to the ant5, which is due to the E-plane beam tilt in this particular frequency range. The beam tilting in the E-plane is caused by the phase shift between the MTS unit cells located along the $+x$ and $-x$ directions. The improved gains for ant3, ant4, ant5, as compared to ant1 and ant2, on the other hand, are due to small separation distance (d in equation (4)) between the radiating current portions, as well as to the decreased dimensions of the radiating unit cells [35]-[36].

To understand the beam tilting for ant4 in the frequency range of 4-5 GHz, Fig. 6(c)-(d) compares the simulated magnitude of the component of E_{x} at 4.9 GHz with that of ant5, whereas Fig. 6(a)-(b) compares the simulated co-polarization (copol) and X-pol radiation patterns in the E- and H-planes of ant3, ant4, and ant5 at the same frequency. As observed, the E-field distribution of ant4 is split into three different directions in the x direction indicated by an arrow and ellipse, while that of ant5 is evenly distributed. The E-field shown using the arrow leads to beam tilt at $\theta = 25°$ in the E- plane, whereas the one illustrated using the ellipse leads to the (SSL), as seen in Fig. 6(a). On the contrary, it is clear that at this frequency, ant5 has symmetric beams in both the E- and H-planes due to the phase tuning introduced by L_{d}. By increasing L_{d}, the difference in the current path ($\nabla \mathrm{P} = P_1 - P_2$) between the MTS elements placed in the $+x$ and $-x$ directions become negligible, as shown in (5), leading to stable boresight patterns.

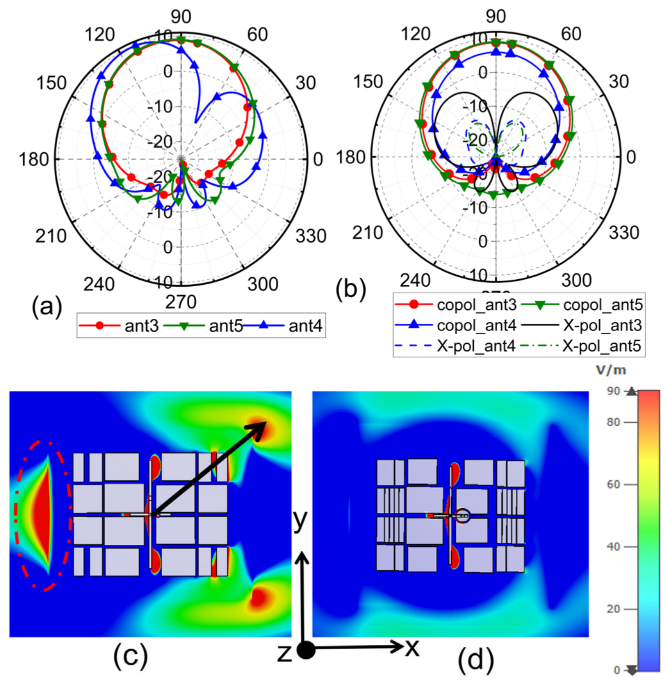

Fig. 6. (a) E-plane Copol; (b) H-plane Copol and X-pol patterns at 4.9 GHz of ant2, atn3, and ant4, respectively. Note that E X-pol is very low for all antennas; therefore, is not shown. (c) and (d) display the magnitude of E_x component of ant3 and ant4, respectively.

$$\nabla\psi = \frac{2\pi\nabla P}{\lambda_0} \tag{5}$$

In equation (5), λ_0 represents the wavelength at a particular frequency within the IBW. It is clear from equation (5) that the phase shift among the MTS unit cells depends on (∇P) and λ_0. Therefore, ($\nabla\psi$) can be varied by either lengthening the current path of the elements located along the $+x$ direction (increasing L_{d}) or changing the size of the elements (λ_0). Doing so will result in stable broadside gain and radiation patterns shown in Figs. 5(a), 6(a)-(b), and 7(a)-(d), respectively. Note also in Fig. 6(b) that at this particular frequency, ant3 has a relatively high X-pol in the H-plane as compared to ant4 and ant5, which may be attributed to the diffraction of the SW at the edges of the finite size ground plane, as shown in Fig. 6(c). On the contrary, by introducing L_{d} and unequal size unit cells, the resulting MTS structure becomes non-uniform, resulting in a well-controlled surface current distribution, as demonstrated in Figs. 6(d) and 14(b). The non-uniform MTS is known to realize the high gain and low X-pol [7], [10] compared to the uniform ones.

It is critical to note here that the radiation patterns of ant5, as shown in Fig. 7(a)-(d), resemble those of the classical magneto-electric dipole antennas [31] in terms of the identical 3-dB

This article has been accepted for publication in a future issue of this journal, but has not been fully edited. Content may change prior to final publication. Citation information: DOI 10.1109/TAP.2020.3027042, IEEE Transactions on Antennas and Propagation

beamwidth in the E- and H-planes, high FBR and low X-pol. For instance, at 4.4 GHz, 5 GHz, 5.5 GHz, and 6 GHz, the proposed antenna achieved 3-dB beamwidths in the E- and H-planes of 73.4° and 73.2°, 65.2° and 65.3°, 56.1° and 54.9°; and 51.7° and 44.6°, respectively. These radiation patterns resemblances are because the feed structure used in this work can be regarded as a thin strip crossed dipole (electric dipole), whereas the metasurface unit cells can be considered magnetic dipoles, and together they form a thin profile printed magneto-electric (ME) dipole antenna, as explained below.

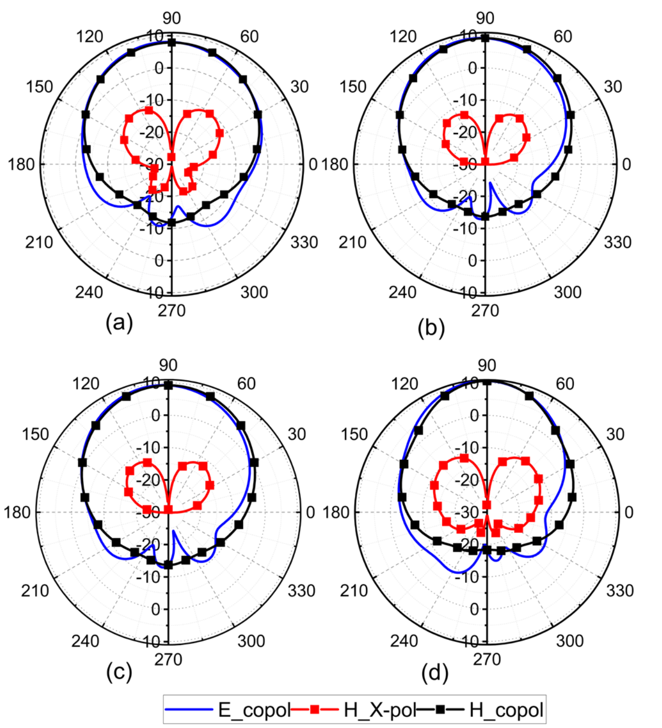

Fig. 7. Simulated E- and H-planes radiation patterns for ant5 (proposed) at 4.4, 5, 5.5 and 6 GHz, respectively. X-pol in the E-plane is extremely low; hence, it is not shown.

D. *The Proposed Antenna (ant5) Performance Analysis*

According to the definition in [31], a complementary antenna (or Huygens's source) comprises an electric (E) dipole and magnetic (M) dipole placed orthogonally and excited simultaneously. From the cavity model, it is known that the microstrip patch antenna (MPA) radiates as a magnetic source; therefore, it can be used to realize an M-dipole. It is also discussed in [37] that a traditional wire dipole antenna is equivalent to an electric current, implying that it can be used to realize an E-dipole. Moreover, it is shown in [38]-[39] that a cross dipole frequency selective surface (FSS) when illuminated by an electromagnetic (TEM) wave, can be decomposed into perpendicular and parallel conducting strips, as illustrated in Fig. 8(b). The conducting strip parallel to the E-field (or orthogonal to the H-field) is equivalent to an inductor, while that orthogonal to the E-field is equivalent to a capacitor. Their corresponding inductance and capacitance are denoted in Fig. 8(c) as L_{di} and C_{di}, respectively. The inductance of the strip is dictated by the length and width of the strip [40]. The capacitance also depends on the strip dimensions, according to the theory of the parallel plate capacitor.

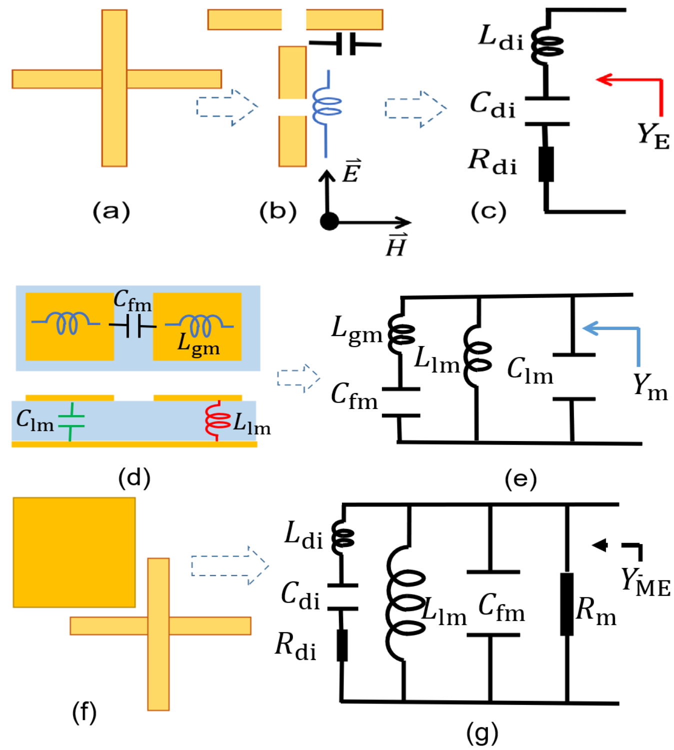

Fig. 8. A simple and intuitive explanation of how the proposed antenna is equivalent to a magneto-electric dipole, and how it achieves a wide IBW. (a) cross dipole; (b) cross dipole decomposed into ∥ and ⊥ components; (c) approximated equivalent circuit model of the crossed dipole; (d) square unit cell with the loading and fringing capacitor and inductor indicated; (e) equivalent circuit model for the unit cell; and (f) and (g) square unit cell and cross dipole combined, along with its approximated circuit model.

The equivalent circuit model shown in Fig. 8(c) can be used to estimate the resonance behavior of the crossed dipole [31]. The resistance, R_{di}, is introduced to account for the radiation from this element. Furthermore, according to [10] and [19], the metasurface unit cell can be modeled using the equivalent circuit model illustrated in Fig. 8(e). Where L_{gm}, C_{fm}, C_{lm} and L_{lm} denote, respectively, the inductance associated with a unit cell, fringing capacitance due to the coupling between adjacent cells, the loading capacitance between the unit cell and the ground, and the grounded dielectric inductance. The Resistance R_{m} is once again introduced to take into account the radiation from the unit cell. C_{fm} and L_{lm} can be estimated using expressions available in [41], while L_{gm} can be calculated using the formula in [10]. By neglecting C_{lm} and L_{gm}, the equivalent circuit shown in Fig. 8(g) can be used to provide insight into the resonant behavior of the proposed magneto-electric dipole antenna [31]. The input admittance Y_{i} of the circuit is:

$$Y_i = \left[\frac{1}{R_{\mathrm{di}} + j\left(\omega L_{\mathrm{di}} - \frac{1}{\omega C_{\mathrm{di}}}\right)}\right] + \left[\frac{1}{R_{\mathrm{m}}} + j\left(\omega C_{\mathrm{fm}} - \frac{1}{\omega L_{\mathrm{lm}}}\right)\right]$$

$$\left[\frac{1}{R_{\mathrm{di}}} + \frac{1}{R_{\mathrm{m}}}\right] - j\left[\left(\omega L_{\mathrm{di}} - \frac{1}{\omega C_{\mathrm{di}}}\right)\frac{1}{R_{\mathrm{di}}^2} - \left(\omega C_{\mathrm{fm}} - \frac{1}{\omega L_{\mathrm{lm}}}\right)\right] \quad (6)$$

This article has been accepted for publication in a future issue of this journal, but has not been fully edited. Content may change prior to final publication. Citation information: DOI 10.1109/TAP.2020.3027042, IEEE Transactions on Antennas and Propagation

It is clear that the imaginary part of (6) is canceled out if the following expression is met

$$\begin{cases} C_{\mathrm{di}}L_{\mathrm{di}} = L_{\mathrm{lm}}C_{\mathrm{fm}} \\ R_{\mathrm{di}}^2 = L_{\mathrm{di}}/C_{\mathrm{fm}} \end{cases} \tag{7}$$

The equation (7) can simultaneously be met if the M- and E-dipoles exhibit approximately the same resonance and the resistance R_{di} of the E-dipole is tuned to a value related to the reactive components of the E- and M-dipoles [31]. Moreover, since the two portions of the feed cross dipole behave simultaneously as inductive and capacitive reactance, and the capacitance and inductance of the latter and that of the MTS unit cells depend on the structure dimensions, it can be concluded that the proposed antenna can realize a wide IBW by optimizing its dimensions [31]. It is worth noting that the effects of the feeding coaxial probe and that of the circular stub are not considered in the analysis above. Regarding the FBR of the magneto-electric dipole antenna, it is demonstrated in [31] that the normalized radiation patterns in planes of any ψ are the same and can be estimated using equation (8) below.

$$F(\theta) = \frac{(1+\cos\theta)}{2} \tag{8}$$

It is seen that the magneto-electric dipole antennas yield very low back radiation, since $F(\theta = 180°) = 0$, which confirms the patterns shown in Fig. 7(a)-(d). The lower profile ($0.05\lambda_0$) of the proposed antenna compared to the traditional magneto-electric dipole antennas ($\lambda_0/4$) [31] can be attributed to the in-phase property of the MTS unit cell [37] and [41].

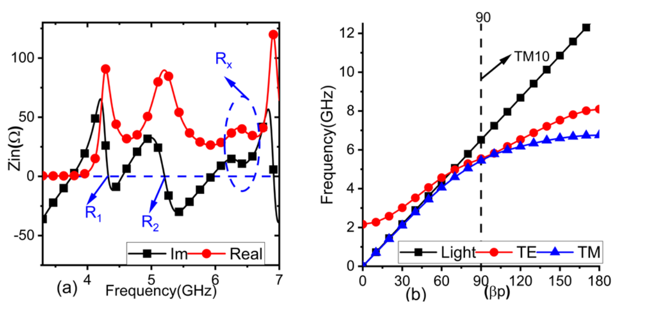

Fig. 9. (a) Simulated input impedance of ant5; (b) simulated dispersion diagram of a unit cell with the solution of equation (3) for $N_{(x,y)} = N_{(x)} = 4$ (ant3).

Fig. 9(a) displays the simulated input impedance of ant5, while Fig. 9(b) shows the simulated dispersion diagram of the MTS unit cell and the solution of (3) for $N_{(x,y)} = N_{(x)} = 4$ (corresponding to ant3). As observed in Fig. 9(a), the proposed antenna obtained two resonance frequencies at 4.32 GHz (R_1) and 5.20 GHz (R_2), which satisfies the negative dispersion slope and $iX = 0$[5],[28]. There is, however, another resonance marked as (R_x) at 6.36 GHz, which fails to meet $iX = 0$. In contrast, as shown in Fig. 2(b), ant1 has only one resonance at 3.81 GHz. Therefore, as is well known that the IBW of a thin profile patch antenna is primarily dictated by the antenna radiation quality factor (Q_r), the wider IBW of ant5 is due to the multiple TM resonances which are closely spaced and the lower quality factor.

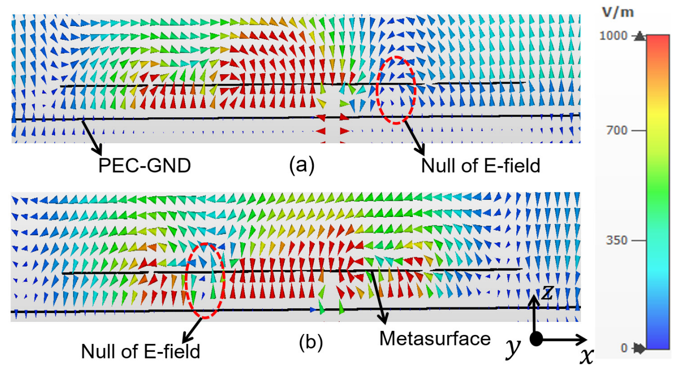

Fig. 10. (a) and (b) simulated E-fields at 4.32 GHz and 5.20 GHz of the proposed antenna (ant5), respectively.

Fig. 10(a)-(b) illustrates the simulated E-field vector in the cavity below the MTS unit cells at R_1 and R_2. As shown in Fig. 10(a), at 4.32 GHz, the E-field is mainly concentrated on the left part of the MTS, while the right part has relatively less concentration, and the E-field changes polarity once at the center. Therefore, this mode might be identified as the modified TM10 under the stronger influence of the feeding thin strip crossed dipole. At 5.20 GHz, on the other hand, the E-field vector is almost evenly distributed along both sides of the MTS with one null. Thus, this mode is the TM10 mode. Using the formula (3) [34], ant 3 realizes a resonance of 5.40 GHz, as shown in Fig. 9(b), which is slightly higher than 5.20 GHz in Fig. 9(a), mainly due to the effect of the fringing E-fields.

III. Parametric Study

To illustrate how different antenna geometrical parameters affect its performance while providing the information on how the proposed antenna can be designed, a parametric study is carried out. It is worth noting that throughout the studies, only

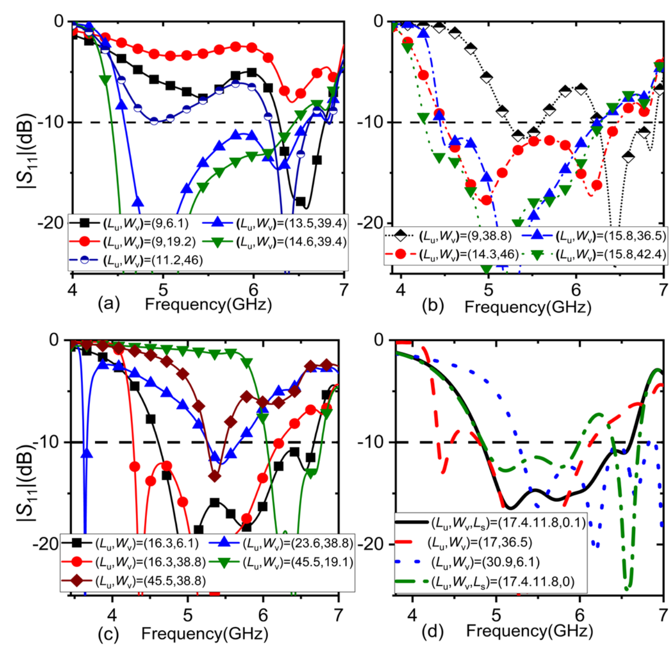

Fig. 11. (a)-(d) the impact of the feed cross dipole lengths, L_u and W_v on ant3 $|S_{11}|$. Unit is mm.

one parameter is varied at a time, while others are kept fixed unless specially indicated. Fig. 11(a)-(d) illustrates the effect of the feeding strip line lengths L_{u} and W_{v} on ant3 $|S_{11}| < -10$ dB IBW. It is clear that with an increase in W_{v}, the operating frequency band moves to the lower edge and the impedance matching improves significantly. This behavior can be attributed to large capacitance and inductance introduced by the two portions of the feeding structure. The increase of the feeding strip lengths L_{u} and W_{v} offers greater inductance and capacitance [40], [42], which in turn respectively lowers and increases the operating band and IBW.

For instance, with $L_{\mathrm{u}} = 15.8$ mm, changing W_{v} to 36.5 and 42.4 mm, varies ant3 $|S_{11}| < -10$ dB IBW from 34.32% (4.44-6.28 GHz) to 38.26 % (4.26-6.28 GHz), respectively, as shown in Fig. 11(b). On the other hand, for $L_{\mathrm{u}} > 30$ mm or <11mm, ant3 yields a very poor impedance matching, as observed in Fig. 11(a)-(c). Better impedance matching is achieved when L_{u} is within $12 - 17$ mm, and good examples are $L_{\mathrm{u}} = 13.5$ mm and $W_{\mathrm{v}} = 39.4$ mm, $L_{\mathrm{u}} = 14.6$ mm and $W_{\mathrm{v}} = 39.4$ mm, $L_{\mathrm{u}} = 16.3$ mm and $W_{\mathrm{v}} = 38.8$ mm; and $L_{\mathrm{u}} = 17.4$ mm and $W_{\mathrm{v}} = 11.8$ mm, which realize IBWs of 34.92% (4.57-6.58 GHz), 36.98% (4.43-6.44 GHz), 36.90% (4.27-6.20 GHz), and 31.5% (4.82-6.61), respectively.

The IBW enhancement obtained when W_{v} is increased is due to the large metasurface area excited by the relatively lengthy feeding strip and improved inductance [40], [42]. Moreover, Fig. 12(a)-(b) illustrates how ant3 $|S_{11}|$ and boresight gain change with increasing the feed lines width (L_{f}), while keeping L_{u} and W_{v} fixed at 16.6 mm and 38.54 mm, respectively. It is obvious that ant3 IBW shifts leftwards as (L_{f}) increases. For example, with L_{f} of 0.36 mm and 0.85 mm, ant3 obtains IBWs for $|S_{11}| < -10$ dB of 31.25% (4.4-6.03 GHz) and 37.75% (4.20-6.14 GHz). While increasing L_{f} further to 1 mm and 1.15 mm lowers the operating band, the impedance matching is poor, as observed in Fig. 12(b).

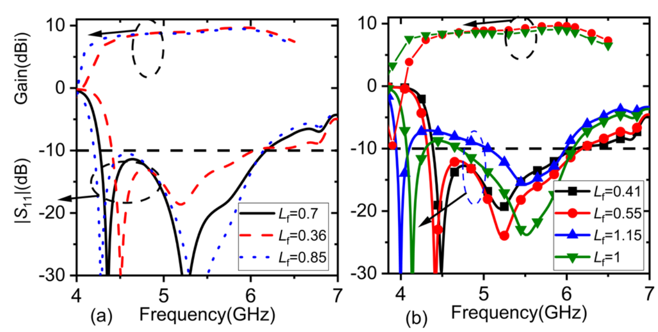

Fig. 12 The effect of the feeding strip line width (L_{f}) on ant3 IBW and boresight gain. Unit is mm.

Over the BWs, the antenna gain variation is insignificant. For L_{f} of 0.55 mm and 0.85 mm, ant3 gain variations are 7.45-9.65 dBi and 7.20-9.47 dBi over the IBW, respectively. Peak gains of $L_{\mathrm{f}} = 0.36$ mm and $L_{\mathrm{f}} = 1$ mm differ by about 0.7 dB, as illustrated in Fig. 12(a)-(b). The increase in the antenna bandwidth with increasing the feeding strip line width is due to the inherent wideband of thick dipoles. From the above parametric studies, it is clear that the antenna with equal MTS unit cells can obtain an IBW of about 35%, which might not be satisfactory for some applications. To broaden the IBW, unequal size MTS unit cells are used to form ant4 and Fig. 13(a) depicts how the $|S_{11}| < -10$ dB IBW and the boresight gain of ant4 change as functions of L_1 and L_3 for fixed $L_{\mathrm{f}} = 1$ mm, $L_{\mathrm{u}} = 15.8$ mm and $W_{\mathrm{v}} = 43$ mm. The contribution of L_{s} on improving the IBW of ant4 at the upper-frequency band is also indicated. It is worth noting that the antenna with unequal size MTS unit cells has a similar performance trend in the S_{11} when the feed network parameters are alternated; therefore, Fig. 13(a)-(b) shows only the optimum cases.

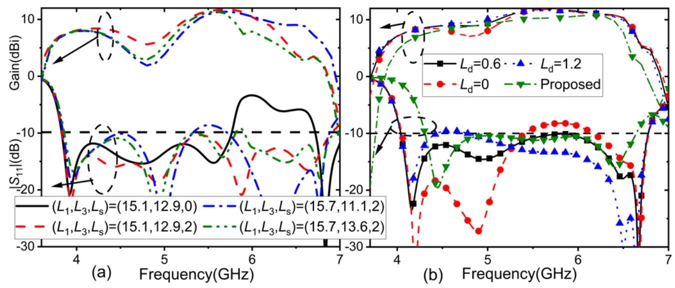

Fig. 13 (a) and (b) Simulated $|S_{11}|$ and boresight gain of ant4 as a function of L_1, L_3, L_{s} and L_{d}, respectively. Unit is mm.

From 13(a), it can be found that the -10 dB IBW of ant4 increases as L_1 increases, and with the introduction of L_{s}. For instance, with $L_1 = 15.1$ and 12.9 mm, varying L_{s} to 0 mm and 2 mm, changes ant4 IBW from 40.41 % (3.83-5.77 GHz) to 57.08 % (3.83-6.89 GHz), respectively, as can be seen in Fig. 13(a). However, in comparison to ant3, ant4 gain degrades both in the mid-band (4-5 GHz) and upper band edge (6-6.9 GHz), mainly due to the mixture of the out-of-phase and in-phase current portions on the MTS unit cells, as demonstrated in Fig. 14(a) and equation (4)[35]. In contrast, by reducing L_3, the 3-dB gain bandwidth improves at the upper band edge, as depicted by the blue line in Fig. 13(a). This increase in the antenna gain can be attributed to the reduced conductor area that supports the out-of-phase current, as illustrated in Fig. 14(a)-(b) and equation (4)[35].

Moreover, Fig. 13(b) shows the influence of L_{d} on ant4 $|S_{11}| < -10$ dB IBW and gain. As seen, in comparison to Fig. 13(a), the -10 dB IBW is simultaneously reduced and shifted rightward, while the gain in the mid-band gets progressively better when L_{d} is increased. The antenna IBW is reduced from 57.22% (3.83-6.90 GHz) to 51.3% (4.02-6.77 GHz), i.e., about 6% IBW reduction is observed. The right shift of the IBW is mainly due to the adjustment of L_{u} for a good impedance matching, as well as to an increase in L_{d} and a decrease in L_3, which reduces the capacitive loading between the MTS unit cells. Nevertheless, the antenna boresight gain, which varies from 7.3 to 11.74 dBi, is now relatively stable across the whole IBW. The disappearance of the dip valley in the boresight in the mid-band is owing to the small phase shift ($\nabla\psi$) between the MTS unit cells located along the $-x$ and $+x$ directions, as can be seen in (5). Although the antenna gain has improved in both the mid and upper bands, the antenna realizes higher SSLs of about 12 dB at frequencies higher than 6 GHz, which affect the

This article has been accepted for publication in a future issue of this journal, but has not been fully edited. Content may change prior to final publication. Citation information: DOI 10.1109/TAP.2020.3027042, IEEE Transactions on Antennas and Propagation

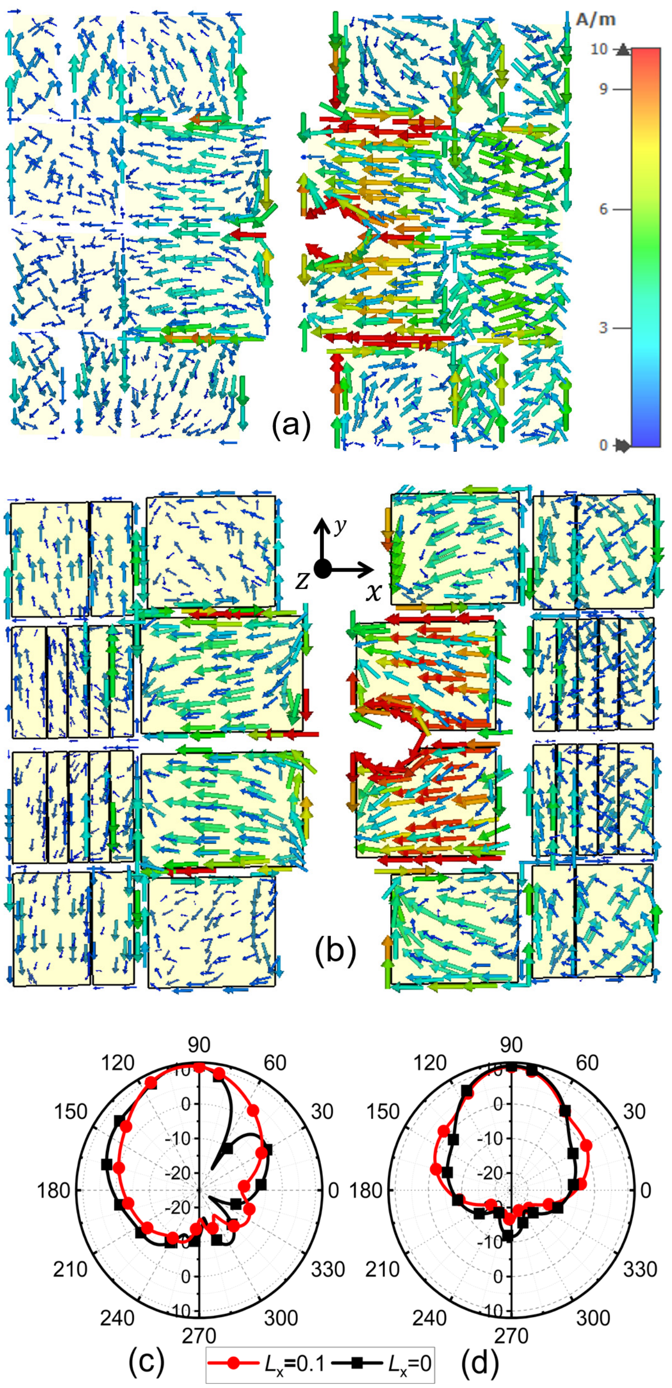

Fig. 14 (a) and (b) simulated surface current at 6.2 GHz for ant5 with and without L_x, while (c) and (d) are the simulated E- and H-planes copol radiation patterns. Note that the hole in the right part of (a) and (b) is the location of the circular stub, which is hidden for clarity.

symmetry of the E-plane radiation patterns, as in Fig. 14(c). To reduce the SSLs in the E-plane, the outer MTS unit cells are sliced into small unit cells using parameter L_x, and Fig. 14 (c)-(d) demonstrates the impact of L_x on the radiation patterns at 6.2 GHz. From Fig. 14(a)-(b), it is seen that with the introduction of L_x, the out-of-phase current on the outer unit cells is weakened, whereas the in-phase current on the central cells is strengthened, leading to radiation patterns with low SSLs shown in Fig.14(c)-(d). The in-phase current distributions for ant4 with L_x is due to the reduced antenna size and the decreased separation distance between the radiating unit cells at higher frequencies, as can be seen in equation (4) [35]-[36]. One should note that the circular hole, which appears in the right part of Fig. 14(a)-(b), corresponds to the position of the circular stub (R), which is hidden for clarity.

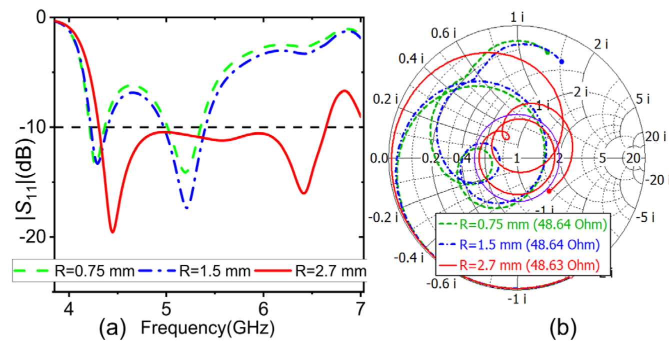

Fig. 15 (a) and (b) effect of the circular matching stub (pad) on the $|S_{11}|$ and the input impedance of ant5, respectively.

Finally, Fig. 15(a)-(b) illustrates the effect of the circular stub (pad) on ant4 impedance matching. It is observed that ant4 impedance matching gets worse with a decrease in R, and with a proper selection of the value of R, a good impedance matching can be achieved. The stub adjusts both the imaginary and real part of the proposed antenna input impedance, as illustrated in Fig. 15(b). Based on the parametric studies above, the design steps for the proposed antenna can be summarized as follows:

- Depending on the lower edge of the operating frequency band, design a square patch using the well-known cavity model-based equations;
- Slice the square patch into four (ant3), and if the required IBW is higher than 35%, set different lengths for the MTS unit cells, as shown in Fig.3 (c), i.e., $1 > 3$ and $2 = 4$);
- Design a feed network based on the substrate parameters, and make it in the form of a crossed dipole. Note that the length and width of the feed network play a very important role in widening the IBW;
- If the patterns and gain are unstable over the $|S_{11}| < -10$ dB BW, use a phase detuning gap in the direction of the feed line axis and depending on the SSLs requirements, slot the outer elements to suppress the SSL at the upper band edge. A circular stub may be placed around the feeding probe to improve the antenna impedance matching.

IV. Experimental Results

To validate the proposed design idea, a prototype of the proposed antenna (ant5) was fabricated and measured. The dimensions of the fabricated antenna are those given in the caption of Fig. 1. Photographs of the fabricated prototype are illustrated in Fig. 16(a), while Fig. 16(b) shows the simulated and measured $|S_{11}| < -10$ dB IBWs and boresight gains as a function of the operating frequency. The simulated -10 dB IBW is 42.85 % (4.29-6.63 GHz), while the measured one is 41.13 %

This article has been accepted for publication in a future issue of this journal, but has not been fully edited. Content may change prior to final publication. Citation information: DOI 10.1109/TAP.2020.3027042, IEEE Transactions on Antennas and Propagation

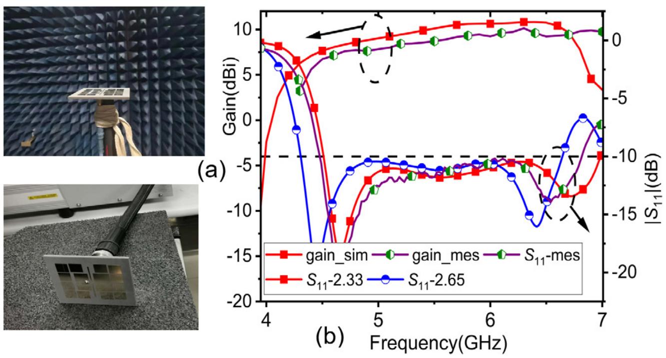

Fig. 16 (a) photographs of the fabricated prototype; (b) simulated (Sim) and measured (mes) $|S_{11}|$ and boresight gain as a function of frequency. The impact of the tolerance in ε_r is also shown.

(4.48-6.80 GHz). Compared to the simulated $|S_{11}| < -10$ dB IBW, the measured one is slightly shifted rightwards due to the minor tolerance in the dielectric constant of the substrate and other fabrication errors, as seen in Fig. 16(b) for $\nabla\varepsilon_r = 0.32$ ($\varepsilon_r = 2.33$).

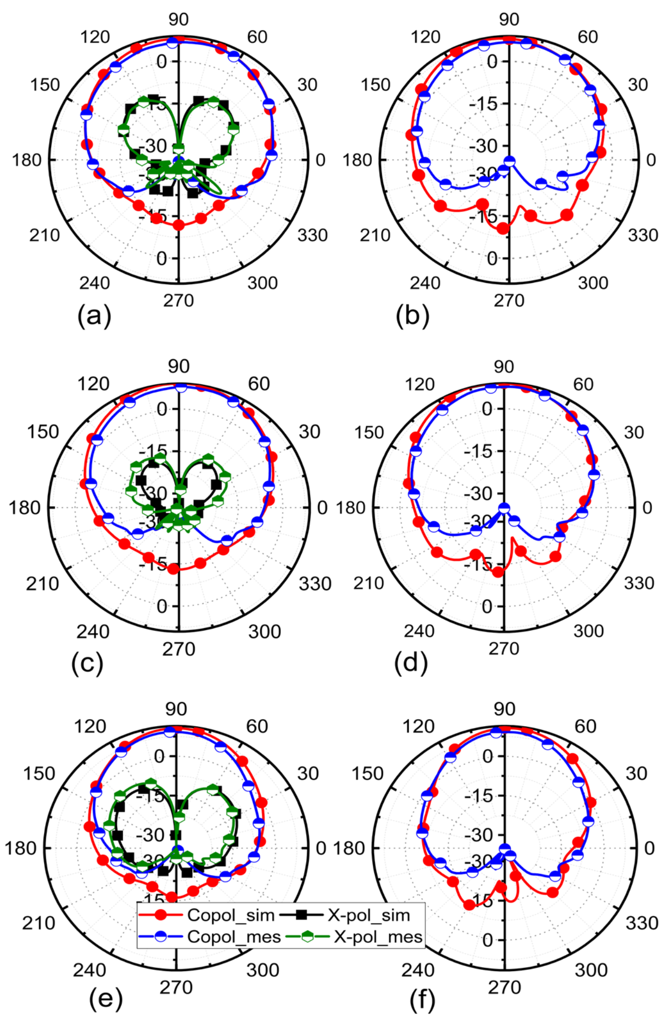

Fig. 17. Simulated (sim) and measured (mes) radiation patterns of the proposed antenna (ant5) at 4.6, 5 and 6 GHz, respectively: left and right columns are H and E planes, respectively. Only X-pol in the H-plane is shown as that of the E-is very low.

Moreover, it is seen in Fig. 16(b) that both the simulated and measured boresight gains exhibit a reasonable agreement. The simulated peak gain is 10.84 dBi at 6.4 GHz, whereas the measured one is 10.14 dBi at 6.3 GHz. The discrepancy between the measured and simulated gains may be attributed to the losses of the connector used in the measurement, which was not taken into account during the simulation. Furthermore, Fig. 17(a)-(f) compared the simulated and measured co-polarization (copol) and (X-pol) radiation patterns in the two principal planes of the proposed antenna at 4.6, 5, and 6 GHz, respectively. A reasonable agreement is achieved between the two results. The measured X-pols in the H-plane are 17 dB below the copol over the whole IBW, whereas those in the E-plane are very low. Therefore, they are not shown in the Figs.

Across the entire IBW, the measured FBRs are higher than 30 dB, which are better than the simulated ones probably due to the supporting material used during the radiation patterns measurement, which increases the size of the ground plane. The simulated radiation and total efficiencies are greater than 98% and 90% across the whole IBW, respectively. Note also that the radiation patterns are stable across the entire IBW, and the measured half power beam widths (HPBWs) are identical in the E- and H-planes as predicted from the simulation

V. Conclusion

This paper presented a single-layer, low-profile, wide $|S_{11}| < -10$ dB IBW 4×4 metasurface-based array antenna. High performances in terms of the $|S_{11}| < -10$ dB IBW, stable boresight radiation patterns and stable gains with a peak gain of 10 dBi, equal E- and H-planes 3-dB beamwidths, low X-pol and high FBR were achieved owing to the use of unequal size AMC unit cells and cross dipole-like feeding structure. Compared to AMC- and MTS-based antennas available in the open literature, the proposed antenna achieved a very low-profile ($0.05\lambda_0$) and uses a single-layer; therefore, it can be easily integrated with other RF and microwave circuits. Moreover, the proposed antenna can be employed to mitigate the high profile ($0.25\lambda_0$) and shaped reflector of the conventional magneto-electric dipole antennas. Because of its salient features, the proposed antenna is an attractive candidate for several modern mobile wireless communication systems, such as mobile base stations and reflector antennas feed.

Acknowledgment

The authors would like to thank USTC information science laboratory center for hardware services, as well as the anonymous editors and reviewers for their insightful comments and suggestions.

References

[1] Garg, R., Bhartia, P. *et al*. Microstrip antenna design handbook. Boston, USA, Artech House, 2001.

[2] R. Q. Lee and K. Lee, "Experimental study of the two-layer electromagnetically coupled rectangular patch antenna," *IEEE Trans. Antennas Propag.*, vol. 38, no. 8, pp. 1298-1302, Aug. 1990.

[3] C. K. Aanandan, P. Mohanan and K. G. Nair, "Broad-band gap coupled microstrip antenna," *IEEE Trans. Antennas Propag.*, vol. 38, no. 10, pp. 1581-1586, Oct. 1990.

[4] M. Clenet and L. Shafai, "Multiple resonances and polarisation of U-slot patch antenna," *Electron. Lett.*, vol. 35, no. 2, pp. 101-103, 21 Jan. 1999.

[5] Ntawangaheza, L. Sun, *et al*., "Thin-Profile Wideband and High-Gain Microstrip Patch Antenna on a Modified AMC," IEEE Antennas Wireless Propag. Lett., vol. 18, no. 12, pp. 2518-2522, Dec. 2019.

[6] D. Chen, W. Yang, *et al*., "High-Gain Patch Antenna Based on Cylindrically Projected EBG Planes," *IEEE Antennas Wireless Propag., Lett.*, vol. 17, no. 12, pp. 2374-2378, Dec. 2018.

[7] W. Yang, D. Chen, *et al*., "High-Efficiency High-Isolation Dual-Orthogonally Polarized Patch Antennas Using Nonperiodic RAMC Structure," *IEEE Trans. Antennas Propag.*, vol. 65, no. 2, pp. 887-892, Feb. 2017.

[8] A. Foroozesh and L. Shafai, "Application of combined electric- and magnetic-conductor ground planes for antenna performance enhancement," Can J. Elect. Comput. Eng., vol. 33, no. 2, pp. 87–98, Spring 2008.

[9] S. Jagtap, A. Chaudhari, *et al*., "A Wideband Microstrip Array Design Using RIS and PRS Layers," *IEEE Antennas Wireless Propag. Lett.*, vol. 17, no. 3, pp. 509-512, Mar. 2018.

[10] Wanchen yang, Wenwuan Che, *et al*." High gain design of a patch antenna using stub-loaded artificial magnetic conductor," IEEE Antennas Wireless propag. Lett., vol. 12, pp. 1172-1175, 2013.

[11] M. Li, R. Wang, J. M. Yasir and L. Jiang, "A Miniaturized Dual-Band Dual-Polarized Band-Notched Slot Antenna Array with High Isolation for Base Station Applications," *IEEE Trans. Antennas Propag.*. doi: 10.1109/TAP.2019.2940471

[12] A. Darvazehban, S. A. Rezaeieh, O. Manoochehri and A. Abbosh, "Two-Dimensional Pattern-Reconfigurable Cross-slot Antenna with Inductive Reflector for Electromagnetic Torso Imaging," *IEEE Trans. Antennas Propag.* doi: 10.1109/TAP.2019.2940617

[13] I. T. McMichael, A. I. Zaghloul and M. S. Mirotznik, "A Method for Determining Optimal EBG Reflection Phase for Low Profile Dipole Antennas," IEEE *Trans. Antennas and Propag.*, vol. 61, no. 5, pp. 2411-2417, May 2013.

[14] J. Zhu, S. Li, *et al*., "Wideband Low-Profile Highly Isolated MIMO Antenna with Artificial Magnetic Conductor," IEEE Antennas Wireless Propag. Lett., vol. 17, no. 3, pp. 458-462, March 2018.

[15] Mateos, R. M., *et al*., "High‐gain wideband low‐profile antenna," Microw. Opt. Technol. Lett., pp. 2615-2619, 2006.

[16] Y. Zhong, G. Yang, *et al*., "Gain enhancement of bow-tie antenna using fractal wideband artificial magnetic conductor ground," Electron. Lett., vol. 51, no. 4, pp. 315-317, 2015.

[17] Wei Liu, Zhi Ning Chen, *et al*., "Metamaterial based low profile broadband mushroom antenna," IEEE Trans. Antennas Propag., vol. 62, no. 3, pp. 1165-1172, Mar. 2014.

[18] Y. M. Pan, P. F. Hu, X. Y. Zhang and S. Y. Zheng, "A Low-Profile High-Gain and Wideband Filtering Antenna With Metasurface," *IEEE Trans. Antennas Propag.*, vol. 64, no. 5, pp. 2010-2016, May 2016.

[19] B. Majumder, K. Krishnamoorthy, *et al*., "Compact Broadband Directive Slot Antenna Loaded with Cavities and Single and Double Layers of Metasurfaces," IEEE Trans. Antennas Propag., vol. 64, no. 11, pp. 4595-4606, Nov. 2016.

[20] W. Liu, Z. N. Chen and X. Qing, "Metamaterial-Based Low-Profile Broadband Aperture-Coupled Grid-Slotted Patch Antenna," *IEEE Trans. Antennas Propag.*, vol. 63, no. 7, pp. 3325-3329, July 2015.

[21] W. E. I. Liu, Z. N. Chen and X. Qing, "Broadband Low-Profile L-Probe Fed Metasurface Antenna with TM Leaky Wave and TE Surface Wave Resonances," *IEEE Trans. Antennas Propag.* doi: 10.1109/TAP.2019.2955629

[22] D. Chen, W. Yang, W. Che and Q. Xue, "Broadband Stable-Gain Multiresonance Antenna Using Nonperiodic Square-Ring Metasurface," *IEEE Antennas Wireless Propag. Lett.*, vol. 18, no. 8, pp. 1537-1541, Aug. 2019.

[23] S. Liu, D. Yang and J. Pan, "A Low-Profile Circularly Polarized Metasurface Antenna With Wide Axial-Ratio Beamwidth," *IEEE Antennas Wireless Propag. Lett.*, vol. 18, no. 7, pp. 1438-1442, July 2019.

[24] W. An, S. Li, W. Sun and Y. Li, "Low-Profile Wideband Microstrip Antenna Based on Multiple Modes With Partial Apertures," *IEEE Antennas Wireless Propag. Lett.*, vol. 18, no. 7, pp. 1372-1376, July 2019.

[25] N. Nie, X. Yang, Z. N. Chen and B. Wang, "A Low-Profile Wideband Hybrid Metasurface Antenna Array for 5G and WiFi Systems," IEEE *Trans. Antennas Propag.* doi: 10.1109/TAP.2019.2940367

[26] Z. Liang, J. Ouyang and F. Yang, "Low-profile wideband circularly polarised single-layer metasurface antenna," *Electron. Lett.*, vol. 54, no. 24, pp. 1362-1364, 29 11 2018.

[27] M. Alharbi, C. A. Balanis, *et al*., "Hybrid Circular Ground Planes for High-Realized-Gain Low-Profile Loop Antennas," IEEE Antennas Wireless Propag. Lett., vol. 17, no. 8, pp. 1426-1429, Aug. 2018.

[28] W. Sun, Y. Li, Z. Zhang and P. Chen, "Low-Profile and Wideband Microstrip Antenna Using Quasi-Periodic Aperture and Slot-to-CPW Transition," *IEEE Trans. Antennas Propag.*, vol. 67, no. 1, pp. 632-637, Jan. 2019.

[29] B. Cheng, Z. Du and D. Huang, "A Broadband Low-Profile Multimode Microstrip Antenna," *IEEE Antennas Wireless Propag. Lett.*, vol. 18, no. 7, pp. 1332-1336, July 2019.

[30] M. S. Alharbi, C. A. Balanis and C. R. Birtcher, "Performance Enhancement of Square-Ring Antennas Exploiting Surface-Wave Metasurfaces," *IEEE Antennas Wireless Propag. Lett.*, vol. 18, no. 10, pp. 1991-1995, Oct. 2019.

[31] Zhi Ning Chen, Handbook of antenna technologies. Singapore: Springer Nature Singapore, 2016.

[32] David GeehYun Kim," Design of stripline-fed dual polarization aperture coupled stacked microstrip patch phased array antenna for wideband application," M.S. thesis, Dept. Elect. Eng. Comput. Sci., Texas A&M Univ., USA, Aug. 2010.

[33] ohn R. Ojha and Marc Peters," Patch Antennas and Microstrip Lines, Microwave and Millimeter Wave Technologies Modern UWB antennas and equipment," Igor Minin, IntechOpen, Mar. 2010.

[34] Costa, O. Luukkonen, C. R. Simovski, A. Monorchio, S. A. Tretyakov and P. M. de Maagt, "TE Surface Wave Resonances on High-Impedance Surface Based Antennas: Analysis and Modeling," IEEE Trans. Antennas Propag., vol. 59, no. 10, pp. 3588-3596, Oct. 2011.

[35] J. Anguera, A. Andújar and J. Jayasinghe, "High-Directivity Microstrip Patch Antennas Based on TModd-0 Modes," IEEE Antennas Wireless Propag. Letters, vol. 19, no. 1, pp. 39-43, Jan. 2020.

[36] Q. U. Khan, D. Fazal and M. bin Ihsan, "Use of Slots to Improve Performance of Patch in Terms of Gain and Sidelobes Reduction," IEEE Antennas Wireless Propag. Lett., vol. 14, pp. 422-425, 2015.

[37] Fan Yang and Yahya rahmat, Electromagnetic bandgap structures in antenna Engineering. New York,USA: Cambridge University Press, 2009.

[38] Eliel P. Santos, Jannayna D.B. Filgueira *et.*"Optimization of frequency selective surfaces with crossed dipoles using the Taguchi's method" Journal of microwaves, optoelectronics and electromagnetic applications, Vol. 16, No. 2,pp. 371-384, Jun. 2017.

[39] Mirshahram Hosseinipanah," Analysis, modeling and Design of artificial magnetic conductors," PhD. thesis, Dept. Elect. Eng. Info. Sci., Harbin Institute of Technology, China, Jul. 2010.

[40] K. Sarabandi and N. Behdad, "A Frequency Selective Surface With Miniaturized Elements," IEEE Trans. Antennas Propag., vol. 55, no. 5, pp. 1239-1245, May 2007.

[41] D. Sievenpiper, Lijun Zhang et al. "High-impedance electromagnetic surfaces with a forbidden frequency band," IEEE Trans. Micr. Theory Tech,, vol. 47, no. 11, pp. 2059-2074, Nov 1999.

[42] . Y. Zouaoui, L. Talbi and K. Hettak, "Cross Dipole FSS Bandwidth Enhancement," 2019 IEEE International Symposium on Antennas and Propagation and USNC-URSI Radio Science Meeting, Atlanta, GA, USA, 2019, pp. 947-948.